

Article

Migration Mechanism of Lattice Oxygen: Conversion of CO₂ to CO Using NiFe₂O₄ Spinel Oxygen Carrier in Chemical Looping Reactions

Da Song ^{1,2} , Yan Lin ² , Kun Zhao ², Zhen Huang ^{2,*}, Fang He ^{1,*} and Ya Xiong ³¹ College of Chemistry and Bioengineering, Guilin University of Technology, Guilin 541004, China² Guangzhou Institute of Energy Conversion, Chinese Academy of Sciences, Guangzhou 510640, China³ Guangdong Provincial Key Laboratory of Environmental Pollution Control & School of Environmental Science & Engineering, Sun Yat-sen University, 135 Xingang Xi Road, Guangzhou 510275, China

* Correspondence: huangzhen@ms.giec.ac.cn (Z.H.); hefang@glut.edu.cn (F.H.)

Abstract: CO₂ resourceful utilization contributes to the goal of carbon neutrality. Chemical Looping Dry Reforming (CLDR) has attracted significant attention as a method for converting CO₂ to CO. NiFe₂O₄ oxygen carrier (OC) is found to be a potential material for CLDR. However, the migration process of lattice oxygen, which are critical for the conversion of CO₂ to CO, was not extensively investigated. In this study, the reduction and oxidation degrees of the NiFe₂O₄ were finely modulated in a thermogravimetric analyzer. The lattice oxygen migration mechanism of the NiFe₂O₄ in redox cycles was characterized by means of X-ray diffraction (XRD), transmission electron microscopy (TEM), X-ray photoelectron spectroscopy (XPS), and in-situ Raman. The novelty of this paper is clarifying the release-uptake paths of lattice oxygen during CO₂ resourceful utilization. The result indicates that the concentration gradient between the surface and the bulk drives the diffusion of lattice oxygen. The stabilization of surface lattice oxygen content is attributed to the rapid migration of O anion, which is closely associated with the movement process of Ni particles inward and outward through the spinel bulk. In addition, a highly reactive chemical reaction interface consisting of lattice oxygen and the corresponding metal atoms is always present on the surface of the oxygen carrier and is confirmed by an in-situ Raman and XPS during the whole process of CLDR. The results of this paper offer reference and basis for further development and design of CLDR using spinel OC.

Keywords: chemical looping (CL); oxygen carrier (OC); CO₂ splitting; lattice oxygen; NiFe₂O₄

Citation: Song, D.; Lin, Y.; Zhao, K.; Huang, Z.; He, F.; Xiong, Y. Migration Mechanism of Lattice Oxygen: Conversion of CO₂ to CO Using NiFe₂O₄ Spinel Oxygen Carrier in Chemical Looping Reactions. *Catalysts* **2022**, *12*, 1181. <https://doi.org/10.3390/catal12101181>

Academic Editors: Chuande Huang, Bo Jiang, Xin Tian and Jiawei Hu

Received: 23 September 2022

Accepted: 5 October 2022

Published: 6 October 2022

Publisher's Note: MDPI stays neutral with regard to jurisdictional claims in published maps and institutional affiliations.



Copyright: © 2022 by the authors. Licensee MDPI, Basel, Switzerland. This article is an open access article distributed under the terms and conditions of the Creative Commons Attribution (CC BY) license (<https://creativecommons.org/licenses/by/4.0/>).

1. Introduction

Excessive emission of greenhouse gases (mainly CO₂) by human beings is considered the primary factor leading to global warming. The CO₂ resource utilization, an effective pathway to reduce greenhouse gas emissions, contributes to the goal of global carbon neutrality [1,2]. The chemical looping dry reforming (CLDR) has attracted much attention for converting CO₂ to CO with the aid of oxygen carriers (OC) [3,4]. The CLDR separates a reforming process into three stages: (1) oxygen carrier reduction stage with a hydrocarbon fuel; (2) CO₂ oxidation stage; (3) air oxidation stage. At the reduction stage, the OC is reduced to a metallic state (Me) and meanwhile partially oxidizes the hydrocarbon fuel into high-quality syngas; At the CO₂ oxidation stage, the reduced oxygen carrier in the metallic state (Me) is oxidized by CO₂ to replenish a part of its lattice oxygen to form a metal oxide with lower oxygen content (MeO_{1-x}) and meanwhile CO₂ is converted to CO; At the air oxidation stage, the partially oxygen-recovered OC (MeO_{1-x}) is fully oxidized into its initial state (MeO), as shown in Figure 1. In the reduction stage, many fuels including but not limited to methane can be used as long as the oxygen carrier exhibits enough reactivity with the fuels in the CLDR process such as H₂, CO, pyrolysis gas, etc. Due to the separation of the redox process, CLDR has a few of potential advantages such as inherent

CO₂ separation, highly efficient activation of CO₂ with a minimal energy penalty, and low operating cost [5–8].

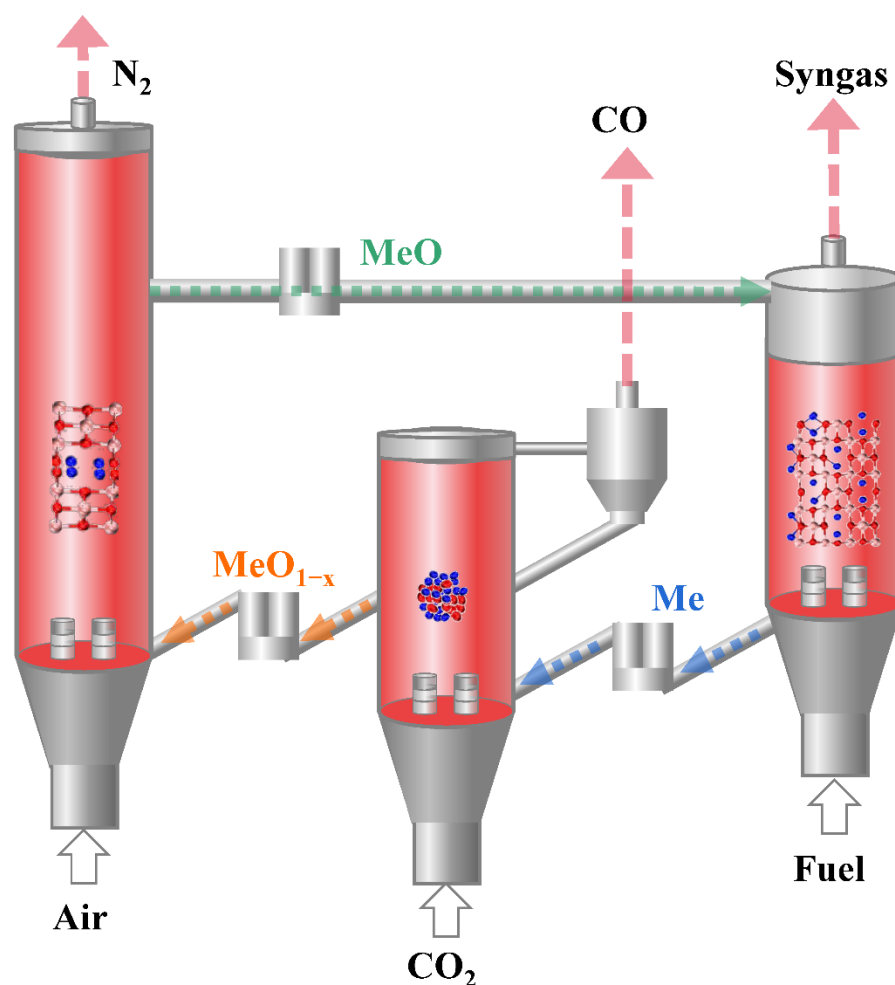


Figure 1. Conceptual illustration of CLDR.

The OC is viewed as the cornerstone of the chemical looping dry reforming [9]. Due to the considerably steady molecule structure and low free energy characteristic of CO₂, the capacity of oxygen carriers to maintain enough high reactivity toward CO₂ reforming is regarded as the most critical issue [10]. Single metal (Co, Ce, Fe, etc.) oxides have been evaluated as oxygen carriers for the CLDR process [11,12]. Among them, Fe-based OC showed the highest CO₂ reducibility. It is also abundant, low-cost, has more oxygen capacity, and is environmentally benign [10]. Thus, Fe-based OCs are considered excellent OC candidates for CLDR [13,14]. In addition, in order to further improve the reactivity of Fe-based oxygen carriers, the use of compound metal oxides (e.g., Ni/Fe, Mn/Fe, Co/Fe, Cu/Fe, and Ca/Fe) as oxygen carrier candidates has been proposed with promising prospect [15–17]. CoFeO_y OC formed from Co-doped Fe-based oxygen carriers exhibited a high syngas yield and maintained stability for 10 cycles in a chemical looping reaction [18]. The synergistic effect of Co doping in ferrite materials to promote Fe reduction. Cu-doped Fe₂O₃ led to the formation of oxygen vacancies, which reduced the reaction activation energy [19], and its reaction rate remained high after 15 cycles. For the methane-carbon dioxide reaction system in CLDR, MnFe₂O₄ OC exhibits the maximum conversion of CH₄ and CO₂ are 63% and 99% [20]. Sun et al. designed a Ca₂Fe₂O₅ OC [21], and the cyclic performance of reduced OC is much better than that of Fe₂O₃. Furthermore, several literatures indicate that the different metals form some unique crystalline structures, such

as spinel (AB_2O_4) [22,23] and perovskites (ABO_3) [24–26], can also obtain some excellent reactivity in CLDR.

In our group, we found that $NiFe_2O_4$ spinel OC is a potential OC for the CLDR of methane [27]. The capability of CO_2 reduction of reduced $NiFe_2O_4$ OC is up to 238 mL/g, which is 2.14 times that of reduced $Fe_2O_3 + NiO$ OC, which gives an average of 185 mL of CO was generated in a single cycle in the 10 successive redox cycles, indicating that the $NiFe_2O_4$ spinel OC shows a relatively stable and good recyclability [28]. As well, the $NiFe_2O_4$ OCs evidently improve the reactivity of Fe-based OCs.

It is known that all the reactions in the three stages of the CLDR involve the migration of lattice oxygen, therefore it is considered the key factor determining the reactivity of OC [29]. However, a lack of fundamental understanding of lattice oxygen migration paths in oxygen carriers limits high-performance oxygen carriers design and development. To date, some exploratory investigations on oxygen ion migration in oxygen carriers have been performed. Chen et al. [30] studied the role of oxygen species in cerium-based oxygen carriers at 450 °C using CH_3SH as a model compound by XPS. they found that the improvement in catalytic stability is closely related to faster migration of bulk phase lattice oxygen. Liu et al. [31] studied the evolution of the active components of copper-iron-based oxygen carriers in the chemical looping combustion of CO, and the results of XPS analysis combined with DFT theory calculation indicated that the bulk phase lattice oxygen tends to migrate outward rather than CO diffusion inward into the particle. Zhao et al. [32] investigated the reaction mechanism of $La_{1.6}Sr_{0.4}FeCoO_6$ oxygen carriers in chemical looping methane steam reforming using XRD and XPS. As well, the results showed that the reaction boundary was fixed on the surface of the oxygen carriers. The oxygen vacancies formed on the surface promoted the migration of lattice oxygen from the bulk phase to the surface. In addition, there are several literatures to discuss the oxygen transfer mechanisms, especially using the density functional theory (DFT) method [33,34]. But there is still a lack of in-depth and systematic understanding of lattice oxygen migration in the bulk of oxygen carriers. As well, experimental investigations on the lattice oxygen transfer in spinel OCs were not extensively investigated. It's rarely found the studies on migration mechanism of lattice oxygen in CLDR to achieve CO_2 resource utilization. Thus, the investigations on release-recovery paths of lattice oxygen are of great significance for understanding the oxidation–reduction reaction mechanisms of OCs.

In order to clarify the release-uptake paths of lattice oxygen during the CLDR process, a thermogravimetric analyzer (TGA) is used to control the reduction degree and oxidation degree of OCs. The migration of lattice oxygen and the evolution of active components during chemical looping reactions were studied by means of XPS, XRD, TEM-EDS, and in-situ Raman. The results of this paper offer reference and basis for further development and design of CLDR using spinel OC.

2. Results and Discussion

2.1. XRD Analysis

2.1.1. Crystalline Phase Evolution of the OC in Reduction

The changes in XRD patterns of OC in the reduction stage are shown in Figure 2. The XRD patterns of the as-synthesized OC showed 12 characteristic peaks, which were found to be in perfect agreement with the standard $NiFe_2O_4$ card 00-054-0964 indicating that the as-synthesized OC by the sol-gel method is pure $NiFe_2O_4$ spinel. When the oxygen carrier was reduced by CO for 5 min, two small Ni peaks (card: 03-065-0380, marked as C) are observed. It indicates that NiO in the $NiFe_2O_4$ is firstly reduced by releasing lattice oxygen and separated from the spinel structure to form free metallic Ni. Another phenomenon was observed in that the rest of the characteristic peaks were slightly broadened and weakened due to a part of $NiFe_2O_4$ converted to $Fe_{3-x}O_4$ (card: 01-086-1355, marked as B). $NiFe_2O_4$ and $Fe_{3-x}O_4$ are both spinel structures, and the XRD spectra of them are very consistent.

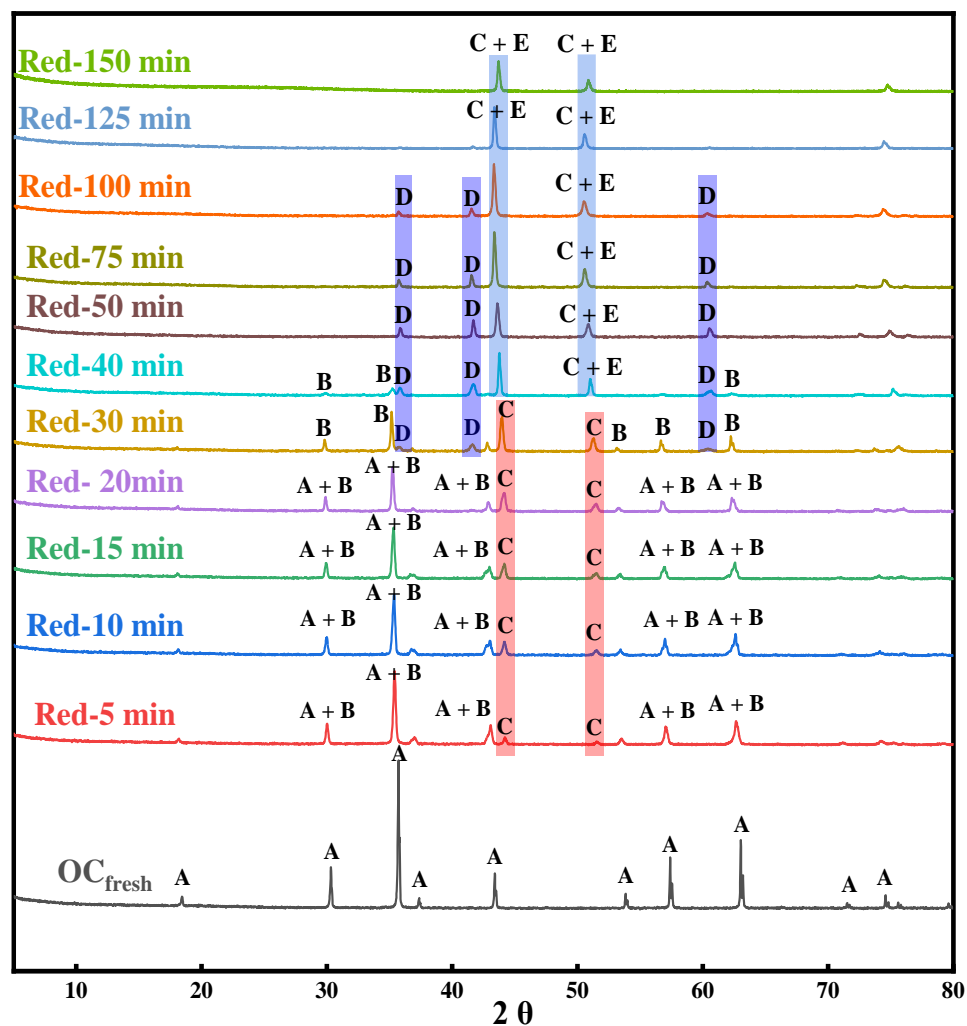


Figure 2. XRD patterns of NiFe_2O_4 OC at different reduction times. (A: NiFe_2O_4 , B: $\text{Fe}_{3-x}\text{O}_4$, C: Ni, D: Fe_{1-x}O , E: Fe).

As the reduction degree deepens, three characteristic peaks of Fe_{1-x}O (card: 01-089-0687) are observed (marked as D). It means that the spinel structure of NiFe_2O_4 and $\text{Fe}_{3-x}\text{O}_4$ gradually collapsed due to Fe^{3+} ions being continuously reduced. Finally, when reduction time is above 100 min, almost Ni and Fe cations are completely reduced into metallic Ni and Fe (card: 96-901-4712).

2.1.2. Crystalline Phase Evolution of the Reduced OC in Oxidation

The metallic Fe and Ni, as the completely reduced product of NiFe_2O_4 OC, show a stepwise oxidation behavior under a CO_2 atmosphere. As well, no apparent carbon deposits were found during the CO_2 oxidation process. As shown in Figure 3.

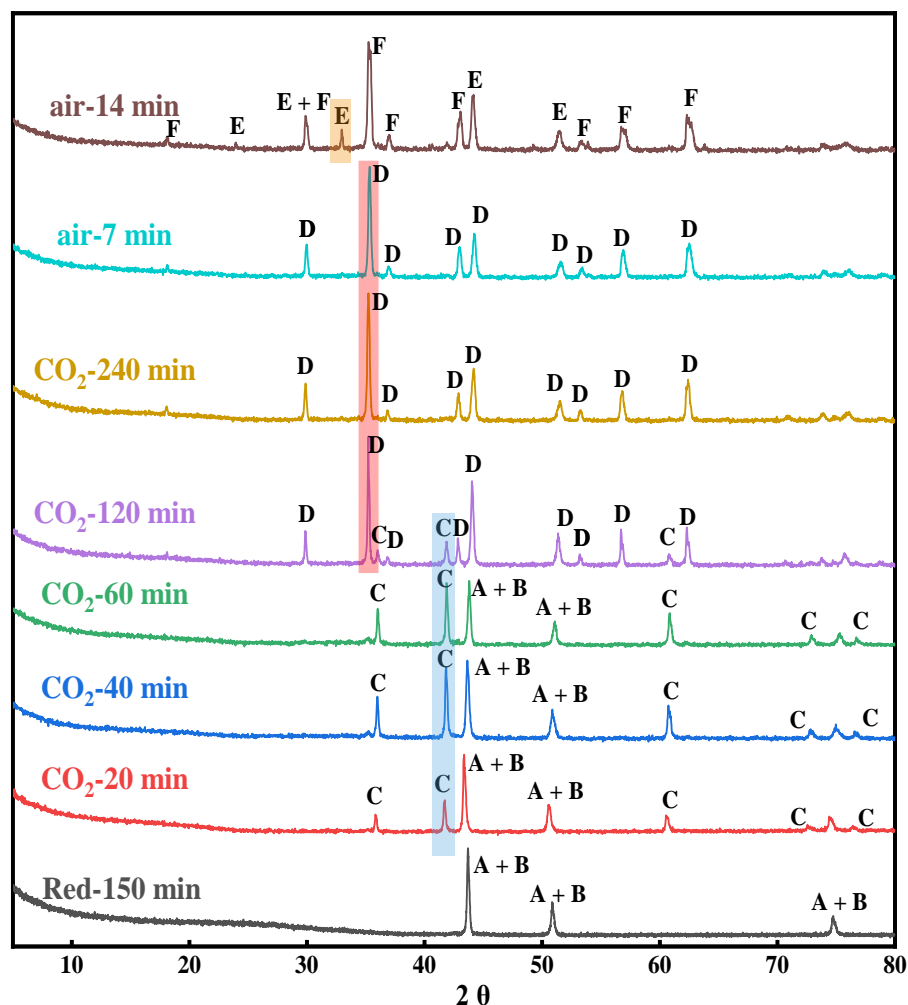


Figure 3. XRD patterns of reduced OC at different oxidation times. (A: Ni, B: Fe, C: Fe_{1-x}O , D: $\text{Fe}_{3-x}\text{O}_4$, E: Fe_2O_3 , F: NiFe_2O_4).

When the oxygen carrier was oxidized by CO_2 for 5 min, a part of metallic Fe is oxidized recovering a fraction of lattice oxygen to form the Fe_{1-x}O phase (marked as C). As the oxidation degree deepens, the characteristic peaks of $\text{Fe}_{3-\delta}\text{O}_4$ are observed (marked as D). It is worth noting that the Ni atoms still exist in the form of metallic Ni due to thermodynamic limitations. It is difficult to replenish all the lattice oxygen under the CO_2 atmosphere owing to the weak oxidation performance of CO_2 . Thus, in order to recover all the lattice oxygen, an air oxidation step is necessary to achieve a whole chemical looping cycle. The OC after CO_2 oxidation is further oxidized by air to recover all the lattice oxygen to form the NiFe_2O_4 phase (marked as F) with spinel structure and a small amount of Fe_2O_3 phase (card: 00-004-0755, marked as E). Although it is difficult to re-oxidize the reduced OC back into its original state, it still exhibits good performance after multi-cycles during the CLDR [27,35].

2.2. XPS Analysis

2.2.1. The Release of Lattice Oxygen

The nature of the oxygen species and the transformation of metal species (Fe and Ni) on the near-surface of OC with reaction time were explored in detail using XPS combined with XRD to further clarify the mechanism of the migration of lattice oxygen. The experimental results are shown in Figures 4 and 5 (the samples analyzed by XPS and XRD are consistent). And the XPS analysis of the O element and the Fe, Ni elements will form a corroboration relation, which strongly supports the migration mechanisms of lattice oxygen during the reduction of NiFe_2O_4 OC.

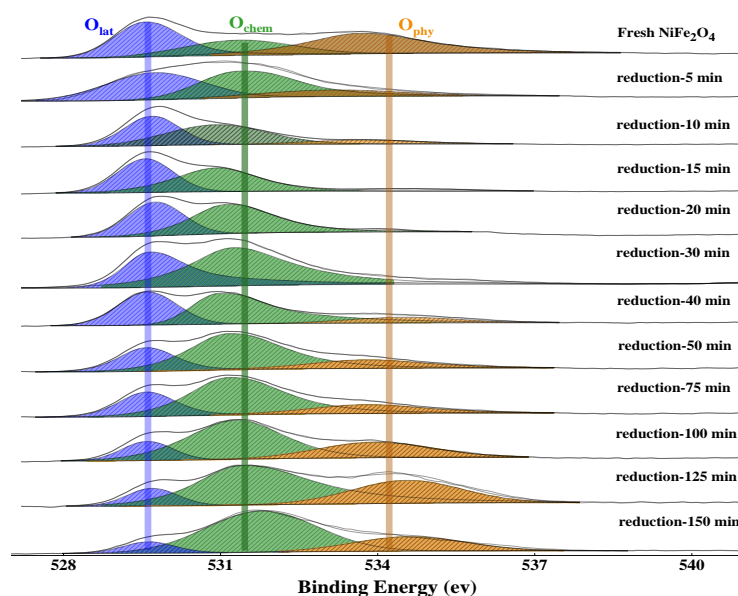


Figure 4. XPS of O1s at different reduction times. (Blue: lattice oxygen, green: chemisorbed oxygen, yellow: physisorbed oxygen).

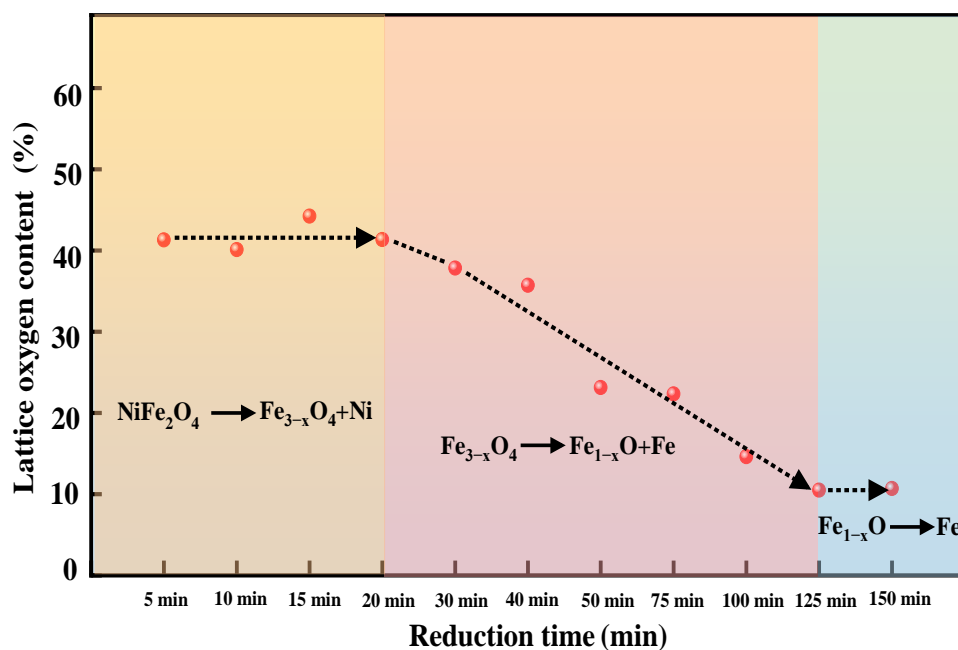


Figure 5. The relative content of lattice oxygen on the surface of OC at different reduction times combined with the evolution of the crystal phase.

The oxygen species on the oxygen carrier surface mainly include lattice oxygen, chemisorbed oxygen, and physisorbed oxygen [30]. The binding energy of lattice oxygen, chemisorbed oxygen, and physisorbed oxygen are 529.0–530.0 eV, 530.0–532.0 eV, and >532.0 eV, respectively [36–40]. Previous literature reported that the different oxygen species can be transformed into each other as follows: $O_2(g) \leftrightarrow O^{2-}(ads) \leftrightarrow O_2^{2-}(ads) \leftrightarrow 2O^-(ads) \leftrightarrow 2O^{2-}(ads) \leftrightarrow 2O^{2-}(lat)$ [41].

As shown in Figure 4, the XPS spectra shows that three oxygen species (lattice oxygen; chemisorbed oxygen; and physisorbed oxygen) can be found on the near-surface of the fresh $NiFe_2O_4$ oxygen carrier particles. At the initial reduction stage (5–20 min), the relative content of physisorbed oxygen gradually decreases with the increase of reduction time (between 5–20 min), which decreases from ~15% at 5 min to ~0% at 20 min. On the contrary,

the relative content of chemisorbed oxygen gradually increases with reduction time, which increases from ~40% at 5 min to ~60% at 30 min. It is worth noting that the relative content of lattice oxygen tends to stabilize at ~40% for the first 20 min at the reduction stage (Figure 5). Meanwhile, the result of XRD shows that the OC maintains the spinel structure and the main phase is $\text{Ni}_{0.6}\text{Fe}_{2.4}\text{O}_4$ and $\text{Fe}_{3-x}\text{O}_4$ during the first 20 min (Figure 5). As well, the oxygen carrier exhibits a fast reduction rate at the initial stage. The results of XRD combined with XPS indicate that the physisorbed oxygen was first consumed from the surface of the oxygen carrier due to the weak adsorption capacity for CO_2/CO . As well, the surface lattice oxygen is easily converted into chemically adsorbed oxygen due to being highly active in the chemical reaction interface [41]. Thus, the relative content of physisorbed oxygen decreased whereas chemisorbed oxygen increased. It also indicates that the conversion rate of the surface lattice oxygen to the chemisorbed oxygen is less than the rate of bulk lattice oxygen migration to the surface, which causes the relative content of surface lattice oxygen to be stable. In other words, three reaction rates determine the changing trend of different oxygen species, namely the consumption rate of chemisorbed oxygen bound to fuel, the conversion rate of surface lattice oxygen to chemisorbed oxygen, and the migration rate of bulk lattice oxygen to the surface, respectively. In the initial stage of the reduction reaction, the migration rate of bulk phase lattice oxygen to the surface is fairly rapid due to the presence of a large amount of lattice oxygen in the bulk of OC and the concentration gradient between the surface and the bulk. This process is accompanied by a part of the Ni element in OC being reduced into free metallic nickel and divorces from the spinel lattice of the NiFe_2O_4 . As well, it also caused the gas-solid reaction interface of was fixed at the surface of the oxygen carrier. Hence, the reaction pathway can be described as follows: CO is firstly adsorbed at the active sites on the surface of the OC particles and then it combines with chemically adsorbed oxygen at the reaction interface to form CO_2 or CO_3^{2-} . The surface lattice oxygen is rapidly and continuously converted into the chemically adsorbed oxygen, meanwhile, the bulk lattice oxygen rapidly migrates to the surface of the spinel structure to replace the consumed lattice oxygen at the initial stage of the reduction reaction. Thus, we inferred that as Ni migrates outward to the particle surface, promoting oxygen vacancies formation and the diffusion of lattice oxygen. It finally leads to a fast rate and the stabilization of the surface lattice oxygen content at the initial reduction stage.

In the intermediate stage of the reduction reaction (20–125 min), the relative content of lattice oxygen gradually decreases with the increase of reduction time, which decreases from ~40% at 20 min (Main phase: $\text{Fe}_{3-x}\text{O}_4$) to ~10% at 125 min (Main phase: metallic Fe and metallic Ni), and then it gradually tends to stabilize (Figure 5). Whereas, the content of physisorbed oxygen gradually increases from ~0% at 20 min (Main phase: $\text{Fe}_{3-x}\text{O}_4$) to ~25% at 125 min (Main phase: metallic Fe and metallic Ni), and then it is gradually stabilized. It indicates that with the collapse of the spinel structure, the bulk lattice oxygen of OC is continuously consumed. In other words, the rate of migration of bulk-phase lattice oxygen to the surface slows down due to the concentration of the lattice oxygen decreasing gradually.

Interestingly, the XRD and XPS analysis show that even if the NiFe_2O_4 OC is completely reduced to the metallic Ni and Fe phases, which means the bulk lattice oxygen is almost fully consumed, and a fraction of lattice oxygen always appears at the surface of the reduced OC (Figure 5). At the same time, the physisorbed oxygen content of the fully reduced OC (125–150 min) was significantly higher than those of the OC in the initial reduction stage (0–20 min). It indicates that the completely reduced OC, namely the metallic Fe and Ni phase, easily adsorbs CO_2 . As CO_2 is adsorbed on the surface of the reduced OC, a CO_2 -splitting reaction occurs on the active metallic Fe. The O anions extracted from CO_2 transform into surface adsorbed oxygen. Subsequently, the adsorbed oxygen further transforms into lattice oxygen induced by the oxygen vacancies on the surface. These two reactions are represented as R (1) [35] and R (2) [41]. Eventually, the relative concentrations of each oxygen species remain unchanged.





Therefore, an active interface consisting of lattice oxygen and the corresponding metallic ions is maintained during the whole reduction process.

The valence evolution of metal cations has a corroborative relationship with the surface oxygen species, thereby shedding light on the migration mechanism of lattice oxygen. It was reported that the peaks with binding energy at around ~856.2 eV, ~854 eV, and ~852.6 eV are assigned to Ni^{2+} , Ni^0 (metallic Ni), and Ni^0 (Fe-Ni), respectively [42,43]. As shown in Figure 6, only Ni^{2+} peaks can be observed in the XPS spectra of the fresh NiFe_2O_4 OC. After reduction for 5 min, a peak for Ni^0 appears in the Ni 2p spectra, indicating that the metallic Ni phase is formed on the surface at the initial reduction stage. This is consistent with the XRD observations. In the reduction time from 5 to 15 min, the relative content of Ni^{2+} ions decreased significantly reaching zero till 20 min, whereas the Ni^0 content increased rapidly. Combined with the O1s XPS spectra (see Figure 4), it can be observed that physisorbed oxygen decrease is accompanied by the initial reduction stage. Thus, the presence of metallic Ni^0 on the surface probably has no effect on the adsorption capacity of OC for CO_2/CO . It was probably due to thermodynamic limitations that metallic Ni^0 cannot react with CO_2 [22]. After 15 min, the peak of Ni^{2+} disappears. All Ni^{2+} is converted to Ni^0 on the surface.

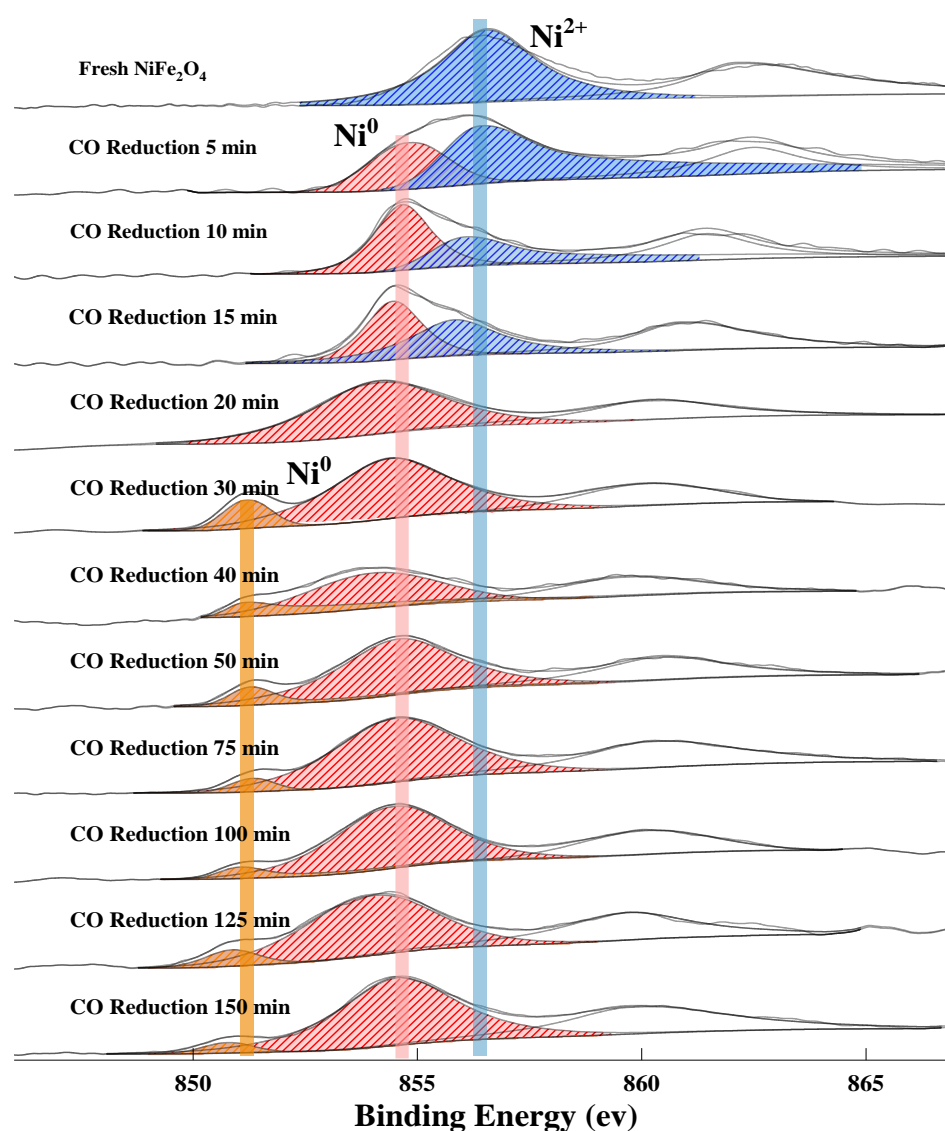


Figure 6. XPS spectrum of Ni 2p 3/2 at different reduction times.

At 30 min, a peak for Fe-Ni alloy appears, corresponding to the formation of metallic Fe with the decomposition of $\text{Fe}_{3-x}\text{O}_4$ to Fe_{1-x}O and Fe. In the reduced NiFe_2O_4 OC, the presence of metallic Fe may create an effect on the electronic structure of metallic Ni. It further indicates that the complete reduction product of OC, is not a simple mixture of Ni and Fe, but a composite with complex space structure, which performance is better than that of the complete reduction product of $\text{NiO} + \text{Fe}_2\text{O}_3$ OC in CLDR [35].

The XPS spectrum of Fe appears in the form of double peaks. As shown in Figure 7. The fresh OC has two Fe^{3+} peaks located at the binding energy of 713.2 eV and 715.5 eV assigned to the spinel NiFe_2O_4 with the structure of the tetrahedron and octahedron structure, respectively. With the reaction proceeding, Fe^{3+} is continuously reduced to Fe^{2+} or Fe^0 . Thus, the Fe^0 , Fe^{2+} and Fe^{3+} peaks appear at ~706.7 eV, ~710 eV and ~713–715 eV, respectively [44]. It is worth noting that the Fe^0 peak cannot be observed on the surface of OC at an initial reduction of 30min. However, the XRD analysis of the crystal phase and the XPS analysis of Ni is similarly observed in the presence of metallic Fe^0 at 30 min. It indicated that Fe^0 is firstly formed inside of the OC particles. In other words, the lattice oxygen tends to migrate to the surface at high temperatures, therefore metallic phase begins to be formed from inside the OC bulk. Similar results have been obtained in other literatures [31,45]. Hence, the metal ions migration pathway can be described as follow: With the release of lattice oxygen, Ni^{2+} was firstly migrated to the surface and reduced to Ni^0 due to the higher reactivity of Ni. Then the lower active Fe^{2+} and Fe^{3+} are subsequently reduced thereby providing lattice oxygen to the fuel on the surface. As the reduction degree deepens, Fe cations begin to be reduced into metallic Fe^0 . The presence of metallic Fe in the bulk creates an effect on the electronic structure of metallic Ni. The surface Fe/Ni ratio of the OC will be analyzed via EDS combined with HRTEM, to further clarify the phenomenon of the migration and enrichment of Fe and Ni atoms during the reduction process. In addition, it was observed that even if OC is completely reduced to the metal phase, the Fe element on the surface is still dominated by Fe^{2+} and Fe^{3+} and only a small amount of Fe^0 . It is due to the strong surface adsorption of the metallic Fe in complete reduced OC, the reaction R (1) is dominated in the later stage of the reaction, thus the relative concentration of surface Fe species remains stable. As well, compared to the initial stage of the reaction, the relative content of physisorbed oxygen gradually increases. The analysis of different elements forms a good corroboration relation, which strongly supports the migration mechanisms of lattice oxygen during the reduction of NiFe_2O_4 OC.

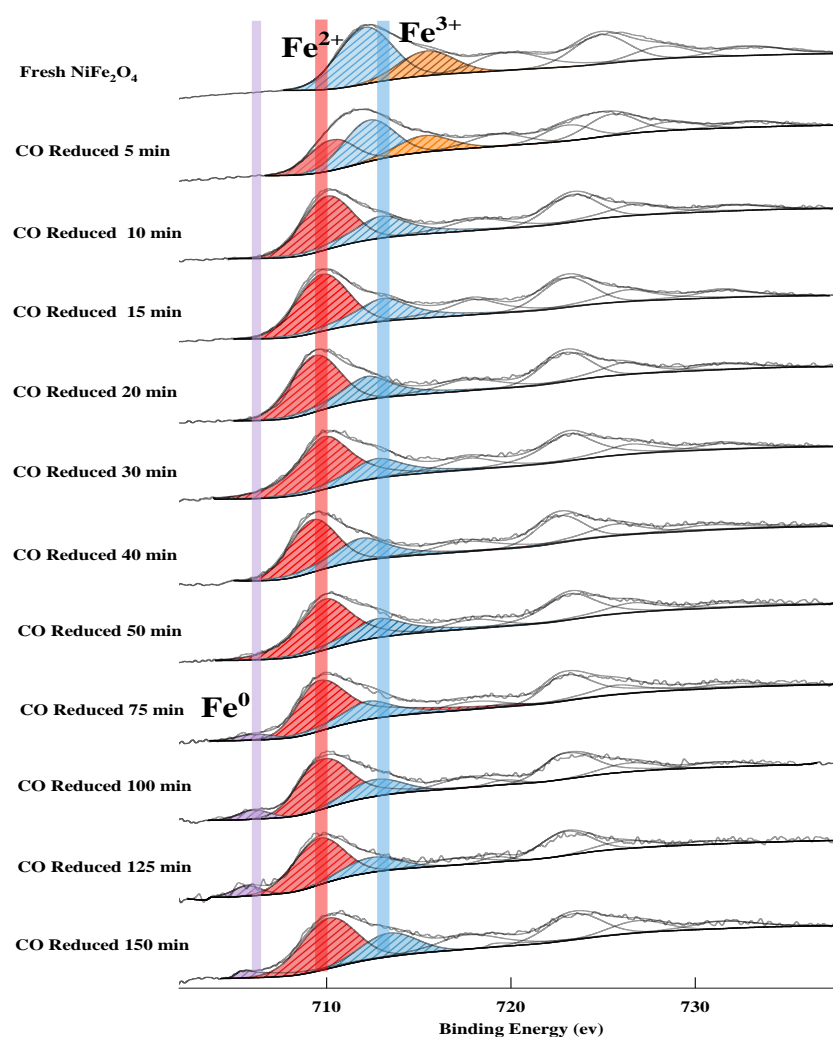


Figure 7. XPS spectrum of Fe $2p\ 3/2$ at different reduction times.

2.2.2. The Uptake of Lattice Oxygen

The O 1s XPS spectra of the oxygen species of the reduced OC re-oxidized in the CO₂-air atmosphere at different oxidation times are shown in Figure 8. It was observed that the lattice oxygen content gradually increases from ~10% at 0 min to ~37% at 240 min of CO₂-oxidation (see Figure 9). However, the physisorbed oxygen content gradually decreases from ~23% at 0 min to ~0% at 120 min. It is noted that the physisorbed oxygen reappeared at oxidization for 240 min. These results should be attributed to a fact that the chemical reaction interface is fixed on the surface of the OC particle during the CO₂ oxidation. If the reaction interface migrates from the surface to the inside. The surface lattice oxygen will reach a maximum at the initial stage of the reaction and then tends to stabilize, rather than gradually increases. In other words, if the surface metal restores all lattice oxygen at the initial stage of the reaction, CO₂ molecules will penetrate through the oxide layer to the interior of the particle to react with metallic Fe. Thus, it indicates that the rate of conversion of the chemisorbed oxygen to the surface lattice oxygen is slightly quicker than the rate of surface lattice oxygen migration to bulk, and then the surface lattice oxygen gradually accumulates. The oxygen concentration gradient between the surface and the bulk continuously drives the lattice oxygen inward transportation to the bulk. In addition, with the recovery of lattice oxygen, the adsorption capacity of oxygen carriers for physisorbed oxygen gradually weakens, which is consistent with the analysis of the reduction process. However, at the end of CO₂ oxidation, a large amount of chemisorbed oxygen can be still observed due to the slower rate of CO₂ splitting and the prolonged

contact between CO₂ and oxygen carriers. Because of the weak oxidizability of CO₂, it is very difficult to recover the entire lattice oxygen for the reduced OC. Thus, an air oxidation process is required to recover the full lattice oxygen of the OC.

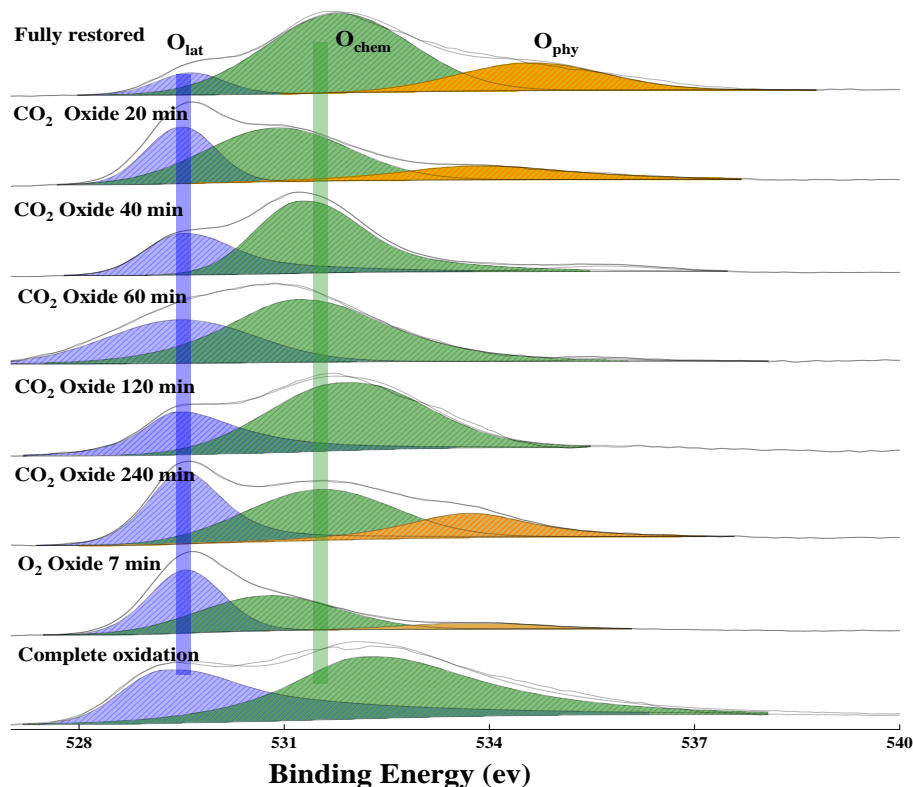


Figure 8. XPS of O1s at different oxidation times. (Blue: lattice oxygen, green: chemisorbed oxygen, yellow: physisorbed oxygen).

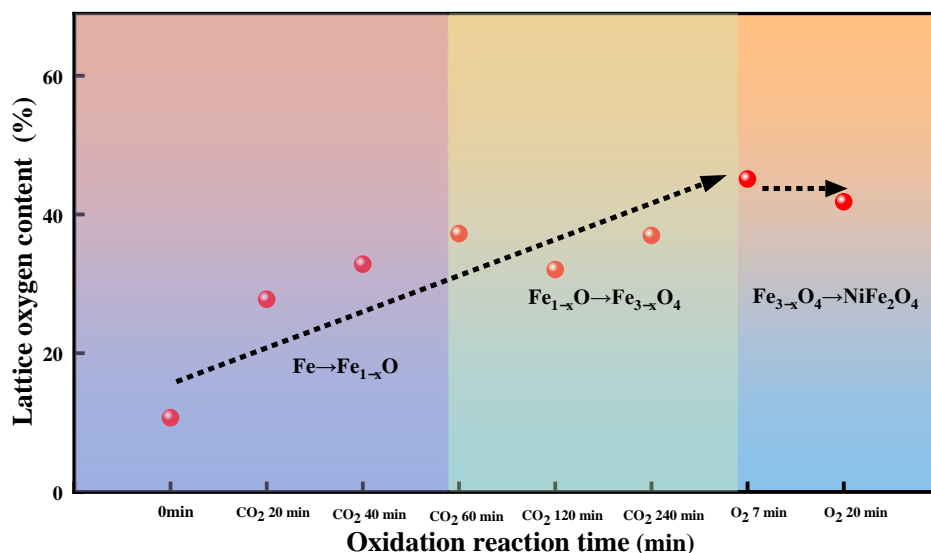


Figure 9. The relative content of lattice oxygen on the surface of OC at different oxidation times combined with the evolution of the crystal phase.

Figure 9 illustrates the lattice contents as a function of oxidation reaction time in air oxidation of the reduced OC. It was observed that the relative content of lattice oxygen increases, which increases from ~37% (at 240 min of CO₂-oxidization) to ~45%, and it

tends to stabilize. The increase in the relative content of lattice oxygen is due to metallic Ni⁰ recovery lattice oxygen on the surface, namely the formation of NiFe₂O₄ species. The stability of the relative content of lattice oxygen is due to the rate of conversion of the chemisorbed oxygen to the surface lattice oxygen is much quicker than the rate of surface lattice oxygen migration to bulk. There is a concentration gradient of lattice oxygen between the surface and the bulk, thus the lattice oxygen is continuously diffused from the surface to the bulk to fill the oxygen vacancies and a relatively stable equilibrium is attained. Thus, the concentrations of lattice oxygen remain stable. Through the above analysis, we infer that the concentration gradient between the surface and the bulk drives the transmission of lattice oxygen to achieve the reduction or oxidation of OC. The migration rate of lattice oxygen is associated with the movement process of Ni particles into and out of spinel bulk.

The Ni 2p XPS spectra (Figure 10) show that the nickel element on the surface of the OC is kept in form of Ni⁰ in the course of CO₂ oxidation due to metallic Ni cannot be oxidized in thermodynamics. The peak of two kinds of Ni⁰ was observed, namely metallic Ni (Ni-Ni) and other kinds of Ni⁰ that the presence of Fe creates an effect on the electronic structure of metallic Ni. The relative content of the two kinds of Ni⁰ fluctuates due to elemental Fe gradually restoring lattice oxygen. During the air oxidation stages, the peak of Ni²⁺ was observed. The result is very consistent with the analysis of oxygen species. In addition, the signal of the Ni element on the surface disappears at 60 min due to the Fe⁰ quickly recovering the lattice oxygen to form Fe_xO and the generated oxide (Fe_xO) can form an oxide film on the surface. The surface Ni atoms are covered by the Fe atoms. As well, the signal of the Ni element is related to the thickness of the surface oxide (Fe_xO). Two peaks of Ni²⁺ were observed for fully oxidized oxygen carriers, which is probably due to the presence of different spatial structures of Fe₂O₃ and NiFe₂O₄.

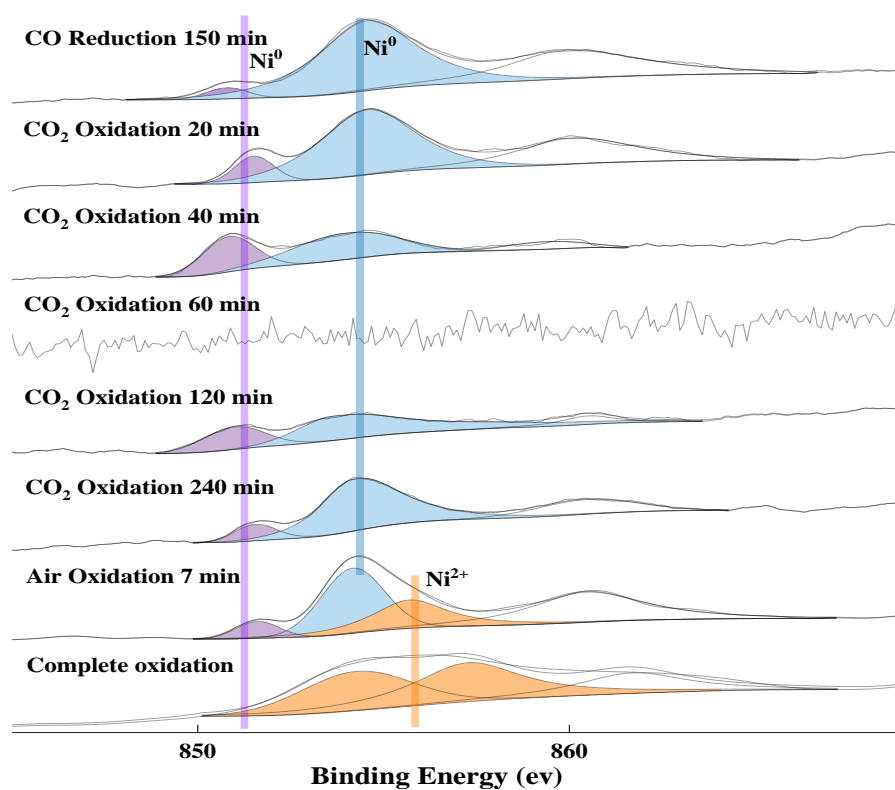


Figure 10. XPS spectrum of Ni 2p 3/2 at different oxidation times.

As shown in Figures 7 and 11, the Fe element in the completely reduced OC is mainly in form of Fe²⁺, Fe³⁺, and a minor amount of Fe⁰. As the reduced OC is oxidized, the Fe⁰ and Fe²⁺ are continuously oxidized into Fe³⁺. When the OC is oxidized by CO₂ for above 20 min, the XPS peak of Fe⁰ disappears. After CO₂-oxidation for 240 min, the Fe element

in the reduced NiFe_2O_4 OC can be reoxidized into Fe_3O_4 by such a weak oxidant, CO_2 . In the completely oxidized OC, the surface Fe element of OC has two Fe^{3+} peaks due to the complex spatial structure of the NiFe_2O_4 and Fe_2O_3 particles.

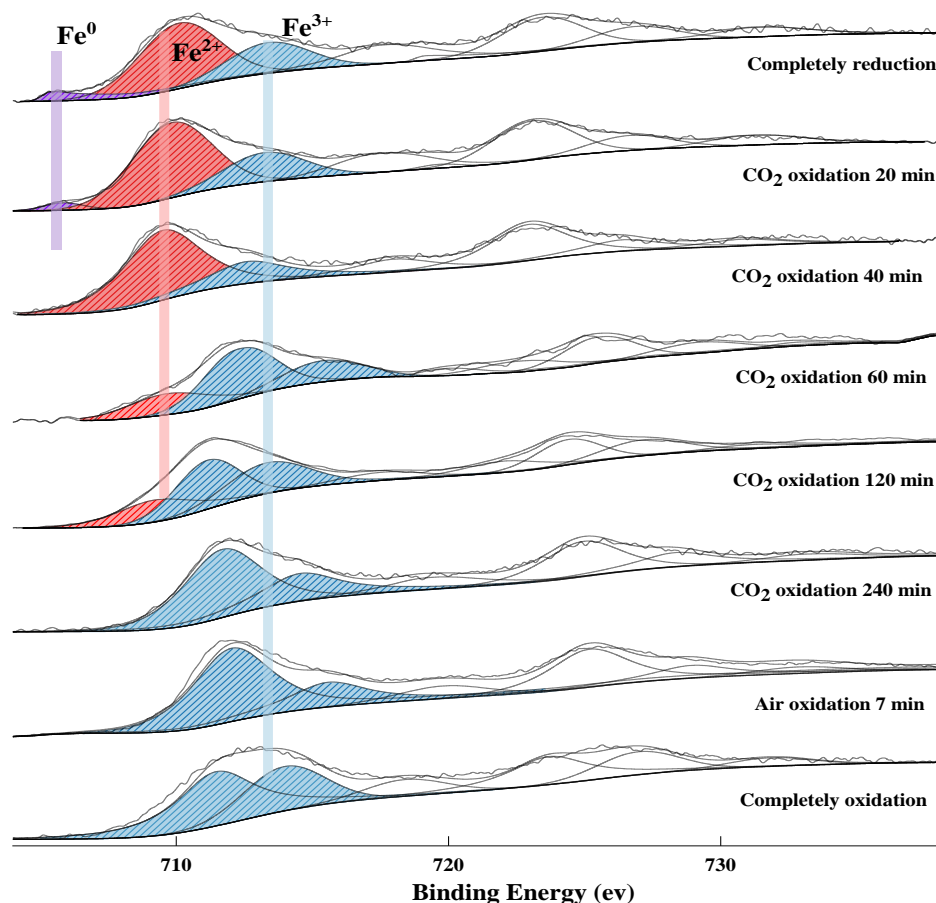


Figure 11. XPS spectrum of Fe $2p\ 3/2$ at different oxidation times.

2.3. In Situ Raman Analysis

The vibrations changes of the chemical bonding in the course of redox reactions on the surface of the OC were studied via in-situ Raman. Compared to non-in situ characterization, in-situ characterization makes it easier to obtain the real results of the materials. As shown in Figure 12, Raman characterizations show five peaks attributed to NiFe_2O_4 [46]. The strongest peak at $\sim 695\text{cm}^{-1}$ is attributed to the symmetric stretching vibration of the O atom along the Fe-O bond direction. The peak at 481cm^{-1} is attributed to the vibration of the Ni-O bond [47]. The peak at 330cm^{-1} is attributed to the symmetric bending vibration of the Fe-O bond [48,49].

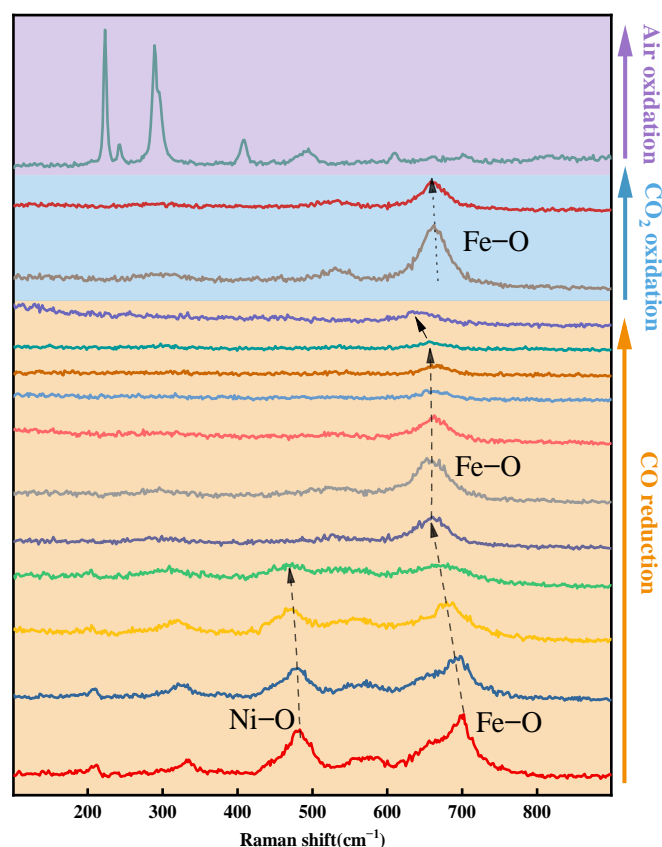


Figure 12. Raman spectra of the redox process of OC.

At the initial stage of the CO-reduction reaction, the peak of Ni-O (481 cm^{-1}) and Fe-O (695 cm^{-1}) display a red shift and gradually becomes weaker, which is due to the formation of oxygen vacancy during lattice oxygen release. Then a very important process is found that the peak of Fe-O (695 cm^{-1}) changes from weak to strong. Meanwhile, the peak of Ni-O (481 cm^{-1}) disappeared. It indicates that the element Ni underwent Ni^{2+} to Ni^0 transition on the surface and Fe atoms combined with remaining lattice oxygen to form a new structure. With the reaction proceeding, the peak of Fe-O gradually becomes weaker from the new structure. However, no matter how long the reduction reaction time lasts, even if the XRD analysis show OC completely reduced to the metal phase, there will always be a peak of Fe-O. The in-situ Raman analysis and the XPS analysis are consistent.

For the OC oxidized by CO_2 , the peak of Fe-O changes from weak to strong. As well, no Ni-O vibration peaks were found. The Raman spectra of the oxygen carrier after air oxidation are different from the fresh samples. But it is very similar to the Raman bands of the pure Fe_2O_3 [49]. It is due to the formation of Fe_2O_3 on the surface of oxygen carriers [50].

2.4. TEM Analysis

The morphology of the fresh NiFe_2O_4 OC, completely reduced OC, reoxidized OC by CO_2 , and completely reoxidized OC by air was investigated by HRTEM, as shown in Figure 13. It is observed that the Ni, Fe, and O elements distribute uniformly throughout the particle in the fresh oxygen carrier. The lattice spacing of the TEM under high magnification was also performed. The crystal forms of the fresh oxygen carrier, $\sim 2.49\text{ \AA}$ of the lattice fringe spacing ascribed to (311) plane of NiFe_2O_4 , can be observed, which are located in the exogenous parts of the oxygen carrier particle. The ratio of surface Fe/Ni ~ 1.83 is very consistent with the theoretical value (Table 1).

Table 1. The relative content of Fe and Ni from EDS mapping.

Element (Atom %)	Fresh OC	Completely Reduced OC	Completely Oxidized OC by CO ₂	Completely Oxidized OC by Air
Fe	47.71%	59.90%	38.19%	37.49%
Ni	25.98%	9.53%	3.67%	3.43%

From Figure 13b, it can be found that the particle size of samples shows an increase due to the collapse of the spinel structure and the enrichment of metallic phases. Small circular particles were observed in distribution inside of the oxygen carrier, which is presumed to be enriched Ni⁰. Under high magnification, a fuzzy boundary located in the exogenous parts of the oxygen carrier particle, and ~ 2.02 Å of the lattice fringe spacing ascribed to (111) plane of metallic Fe⁰, can be observed. A fuzzy boundary probably has a relationship with the highly reactive chemical reaction interface, which consists of lattice oxygen and the corresponding metallic ions. The EDS mapping shows the ratio of surface Fe/Ni ~ 6.28 , which indicates that the surface Ni atoms are covered by the Fe atoms.

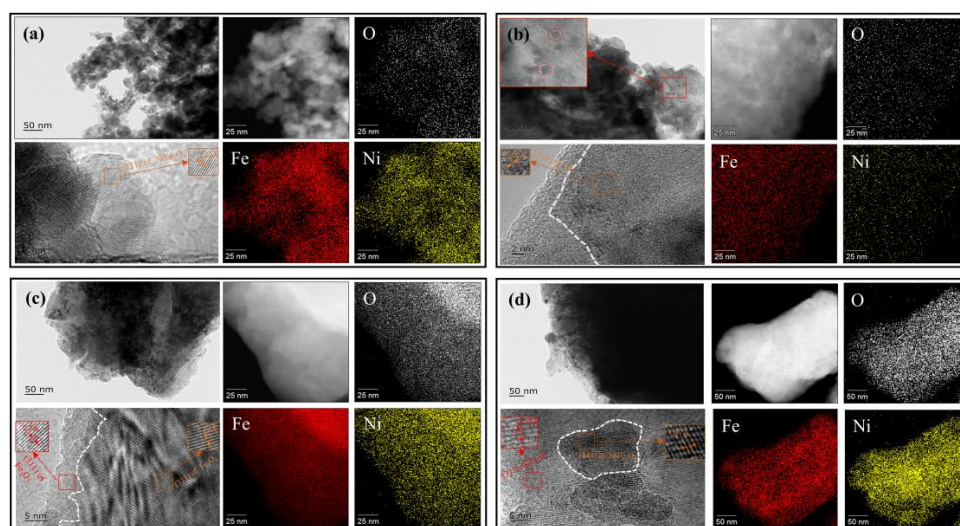


Figure 13. HRTEM and EDS mapping: (a) (Fresh NiFe₂O₄ OC); (b) (Completely reduced OC); (c) (Completely oxidized OC by CO₂); (d) (Completely oxidized OC by Air).

As shown in Figure 13c, many small circular particles were still observed distributed inside of the oxygen carrier. It is probably due to Ni⁰ cannot be oxidized by CO₂. The lattice spacing of Fe₃O₄(311) and a boundary are observed. From Figure 13d, in the middle of the Fe₂O₃(311), there is a layer with the lattice fringe spacing of ~ 1.47 Å related to the (440) plane of NiFe₂O₄. The EDS mapping shows that the ratio of surface Fe/Ni did not return to the original state. It indicates that Fe₂O₃ exists on the surface of the completely oxidized oxygen carrier [50].

According to the above analysis, the potential reaction paths and mechanism of NiFe₂O₄ in the CLDR process can be proposed as shown in Figure 14. It can observe that the process of CLDR of methane consists of a successive three-step chemical looping scheme, where NiFe₂O₄ OC is supposed to: (i) convert various fuels (e.g., CH₄, biomass) to value-added products (e.g., heat, syngas), (ii) reduce CO₂ to produce CO, and (iii) consume oxygen from the air to replenish full lattice oxygen meanwhile sustaining the thermal balance of the system. The chemical reaction interface is fixed on the surface of OC particles (Figure 14). During the oxygen carrier reduction process, the bulk lattice oxygen migrated to the particle surface and converted to adsorbed oxygen, which is consumed by fuel. During the oxygen carrier oxidation process, CO₂ is adsorbed on the particle surface and dissociates into O ions, which are converted from adsorbed oxygen to lattice oxygen and migrate to the bulk. The diffusion of oxygen anions maintains the overall charge neutrality

due to the oxygen chemical potential gradient. It is worth noting that the phase segregation caused by the outward diffusion of metal cations is not conducive to the cyclic stability of oxygen carriers. Adding an inert component to control the movement of active metal atoms is one of the directions worthy of our efforts in the future to achieve better performance. Through the above analysis, we infer that utilizing or controlling the reversible dynamic changes behavior of particles will be an effective means to enhance the reactivity and stability of oxygen carriers in future chemical looping applications.

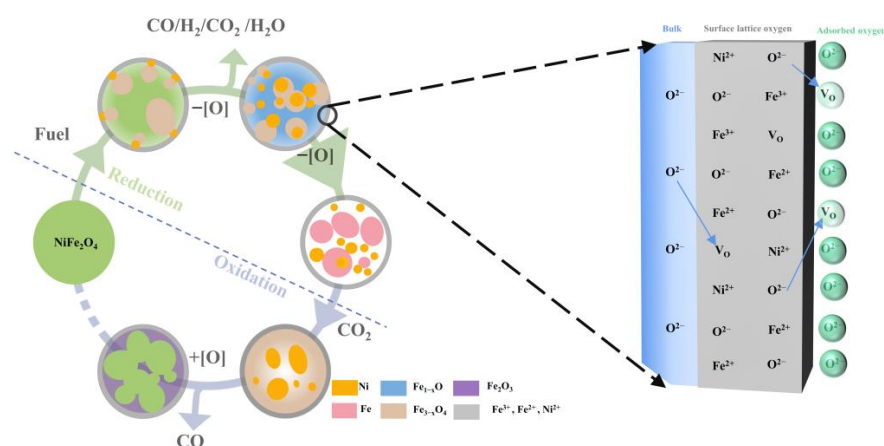


Figure 14. Redox mechanism description in CLDR process.

3. Materials and Methods

3.1. Preparation of Oxygen Carrier

The sol–gel methods were applied to prepare NiFe_2O_4 nanoparticles. Nickel nitrate hexahydrate $[\text{Ni}(\text{NO}_3)_2 \cdot 6\text{H}_2\text{O}]$ (Aladdin, $\geq 99.99\%$) and iron nitrate nonahydrate $[\text{Fe}(\text{NO}_3)_3 \cdot 9\text{H}_2\text{O}]$ (Aladdin, $\geq 99.99\%$) were used as raw materials and dissolved in deionized water, forming 1 M of $\text{Ni}(\text{NO}_3)_2$ solution and 2 M of $\text{Fe}(\text{NO}_3)_3$ solution, respectively. The citric acid (Macklin, $\geq 99.5\%$) with the equivalent molar $\text{Ni}(\text{NO}_3)_2$ was added to the original mixed solution. Subsequently, obtain a pH of 7.5. Finally, the solution was heated at $65\text{--}75\text{ }^\circ\text{C}$ to evaporate 2/3 of the water, and the gel formed when the solution was cooled to room temperature. The precursors were dried in a vacuum evaporator at $120\text{ }^\circ\text{C}$ and calcined for the formation of the ferrite phase in a muffle furnace under an air atmosphere according to the same temperature program. The dried materials were calcined by increasing the temperature from $25\text{ }^\circ\text{C}$ to $400\text{ }^\circ\text{C}$ with a ramp of $8\text{ }^\circ\text{C}/\text{min}$ and keeping at $400\text{ }^\circ\text{C}$ for 2 h. Then the sample was increased to $1200\text{ }^\circ\text{C}$ at a heating rate of $4\text{ }^\circ\text{C}/\text{min}$, and kept at $1200\text{ }^\circ\text{C}$ for 2 h [46].

3.2. Thermo-Gravimetric (TG) Analysis

The three stages of the CLDR experiment are carried out by the STA-409/PC thermogravimetric analyzer, which is produced by NETZSCH, Selb, Germany. The three different gases (CO, CO_2 , and air) flow rates are all set to $100\text{ mL}/\text{min}$. The experimental procedure is as follows: NiFe_2O_4 OC ($m = 150\text{ mg} \pm 0.1\text{ mg}$) was added to the thermogravimetric reactor. the reaction temperature is heated up to $950\text{ }^\circ\text{C}$ at a heating rate of $10\text{ }^\circ\text{C}/\text{min}$ in an inert atmosphere. Then, CO is introduced for the reduction reaction. After the reduction experiment, CO_2 and air is introduced for oxidation reaction, respectively. Obtain 19 samples with different reaction times for subsequent analysis, which are recorded as OC_{fresh} , reduction-5 min, reduction-10 min, reduction-15 min, reduction-20 min, reduction-30 min, reduction-40 min, reduction-50 min, reduction-75 min, reduction-100 min, reduction-125 min, reduction-150 min, CO_2 -oxidation-20 min, CO_2 -oxidation-40 min, CO_2 -oxidation-60 min, CO_2 -oxidation-120 min, CO_2 -oxidation-240 min, air-oxidation-7 min, air-oxidation-14 min, respectively.

3.3. Characterization

3.3.1. X-ray Photoelectron Spectroscopy (XPS)

An X-ray photoelectron spectroscopy technology (XPS, Thermo Fisher Scientific ESCALAB 250Xi, Waltham, MA, USA) was carried out to investigate the valence state of variable metal ions and oxygen species of OCs, with an Al K α X-ray source (1486.6 eV photons) at an operating voltage of 20 kV and a current of 10 mA, respectively.

3.3.2. X-ray Diffraction (XRD)

An X-ray diffractometer (XRD) using 40 kV, 40 mA Cu K α radiation was used to analyze the crystal structure of fresh and reacted samples. XRD measurement scanning rate is 2 °/min from $2\theta = 5\text{--}80^\circ$ with a step size of 0.02°.

3.3.3. In Situ Raman

A Laser Confocal Micro-Raman Spectral System (LabRAM HR800, HORIBA Scientific, Piscataway, NJ, USA) was used to analyze the surface structure of the oxygen carrier. Laser full range of 50 mw, selected a laser probe with a wavelength of 432.521 cm⁻¹. Added NiFe₂O₄ oxygen carrier mass of 100 mg in the in-situ stage, under 20 mL/min inert atmosphere, warmed up at a rate of 50 K/min to 950 °C. When the temperature rises to 950 °C, a gas (the CO reduction and CO₂-air oxidation) is continuously introduced into the reactor, respectively. A total of 20 mL/min CO gas (10 vol%CO, N₂ equilibrium) for reduction. Then switch to CO₂ (10 vol%CO₂, N₂ equilibrium) with a flow rate of 20 mL/min for oxidation reaction after the end of reduction. Finally, pass air (20 mL/min) for strong oxidation.

3.3.4. Transmission Electron Microscopy (TEM)

The microstructure of the sample was analyzed using a high-resolution field emission transmission electron microscope (JEOL 125 JEM-2100F, Tokyo, Japan). EDS energy spectrometer manufactured by American Thermoelectric Noran (Waltham, MA, USA).

4. Conclusions

In this study, we elaborated on the reversible phase transition law of NiFe₂O₄ using the sol-gel method for the preparation of the chemical looping CO₂ splitting process. Then valence evolution of active components of the oxygen carriers was analyzed in detail by XPS. As well, we explained the chemical mechanism of the change in the relative content of different oxygen species. A large number of evidence about bulk lattice oxygen migration was obtained by different characterizations.

A fact was confirmed by an in-situ Raman and XPS that a highly reactive chemical reaction interface consisting of lattice oxygen and the corresponding metal atoms is always present on the surface of the oxygen carrier during the CLDR. In summary, the diffusion of oxygen anions maintains the overall charge neutrality due to the oxygen chemical potential gradient. Oxygen anions move from a high concentration area to a low concentration area, namely the surface lattice oxygen is converted to chemisorbed oxygen and forms oxygen vacancies. The bulk lattice oxygen to the surface and healed the surface vacancy via outward diffusion. The diffusion of metallic Fe and metallic Ni changes the morphology and crystalline structure of OC. The extraordinary performance of NiFe₂O₄ for CLDR is due to the movement of Ni particles into and out of spinel bulk, which promote oxygen migration and diffusion. In the reduction period under CO, a part of the Ni element in OC is first separated from the spinel structure to become the free metallic Ni. It was confirmed that exsolved Ni nanoparticles were not redissolved into the spinel in the oxidation under CO₂, and the active phase (Ni) was dissolved into the matched spinel under an air atmosphere. This understanding of the migration of active metals and lattice oxygen is of great significance for material design for the applications of CLDR, especially through structure design and utilizing the dynamic phase change to stabilize the metal particles. As well, establishing the relationship between the dynamic behavior and performance

of the metal is one of the directions worthy of our efforts in the future to achieve better performance of OC in CLDR; it also can promote the process of CO₂ resource utilization and carbon neutrality goals.

Author Contributions: Conceptualization, D.S. and Y.L.; methodology, Z.H.; software, D.S.; validation, D.S., Z.H. and F.H.; formal analysis, K.Z. and F.H.; investigation, D.S.; resources, Y.X.; data curation, D.S.; writing—original draft preparation, D.S.; writing—review and editing, F.H.; visualization, Z.H.; supervision, Z.H.; project administration, Y.L.; funding acquisition, Z.H. All authors have read and agreed to the published version of the manuscript.

Funding: This research was funded by the National Natural Science Foundation of China (52006224, 52076209, 22179027), the Foundation and Applied Foundation Research of Guangdong Province (2019B1515120022, 2019A1515110828, 2020A1515110138, 2021A1515010459, 2022B1515020045), the Joint Fund of the Yulin University and the Dalian National Laboratory for Clean Energy (2021021), Guangxi Natural Science Foundation (2018GXNSFDA281005), Youth Innovation Promotion Association, CAS (2019341).

Conflicts of Interest: The authors declare no conflict of interest.

References

1. Donat, F.; Müller, C.R. CO₂-free conversion of CH₄ to syngas using chemical looping. *Appl. Catal. B Environ.* **2020**, *278*. [[CrossRef](#)]
2. Wang, J.; Huang, L.; Yang, R.; Zhang, Z.; Wu, J.; Gao, Y.; Wang, Q.; O'Hare, D.; Zhong, Z. Recent advances in solid sorbents for CO₂ capture and new development trends. *Energy Environ. Sci.* **2014**, *7*, 3478–3518. [[CrossRef](#)]
3. Kortlever, R.; Shen, J.; Schouten, K.J.P.; Calle-Vallejo, F.; Koper, M.T.M. Catalysts and Reaction Pathways for the Electrochemical Reduction of Carbon Dioxide. *J. Phys. Chem. Lett.* **2015**, *6*, 4073–4082. [[CrossRef](#)]
4. Adanez, J.; Abad, A.; Garcia-Labiano, F.; Gayan, P.; de Diego, L.F. Progress in Chemical-Looping Combustion and Reforming technologies. *Prog. Energy Combust. Sci.* **2012**, *38*, 215–282. [[CrossRef](#)]
5. Kim, J.; Johnson, T.A.; Miller, J.E.; Stechel, E.B.; Maravelias, C.T. Fuel production from CO₂ using solar-thermal energy: System level analysis. *Energy Environ. Sci.* **2012**, *5*, 8417–8429. [[CrossRef](#)]
6. Ekström, C.; Schwendig, F.; Biede, O.; Franco, F.; Haupt, G.; de Koeijer, G.; Papapavlou, C.; Røkke, P.E. Techno-Economic Evaluations and Benchmarking of Pre-combustion CO₂ Capture and Oxy-fuel Processes Developed in the European ENCAP Project. *Energy Procedia* **2009**, *1*, 4233–4240. [[CrossRef](#)]
7. Meng, W.X.; Banerjee, S.; Zhang, X.; Agarwal, R.K. Process simulation of multi-stage chemical-looping combustion using Aspen Plus. *Energy* **2015**, *90*, 1869–1877. [[CrossRef](#)]
8. Ksepko, E.; Lysowski, R. Reactivity Study of Bimetallic Fe-Mn Oxides with Addition of TiO₂ for Chemical Looping Combustion Purposes. *Catalysts* **2021**, *11*, 1437. [[CrossRef](#)]
9. Hossain, M.M.; de Lasa, H.I. Chemical-looping combustion (CLC) for inherent CO₂ separations—A review. *Chem. Eng. Sci.* **2008**, *63*, 4433–4451. [[CrossRef](#)]
10. Tang, M.C.; Xu, L.; Fan, M.H. Progress in oxygen carrier development of methane-based chemical-looping reforming: A review. *Appl. Energy* **2015**, *151*, 143–156. [[CrossRef](#)]
11. Galvita, V.V.; Poelman, H.; Bliznuk, V.; Detavernier, C.; Marin, G.B. CeO₂-Modified Fe₂O₃ for CO₂ Utilization via Chemical Looping. *Ind. Eng. Chem. Res.* **2013**, *52*, 8416–8426. [[CrossRef](#)]
12. Galvita, V.V.; Poelman, H.; Detavernier, C.; Marin, G.B. Catalyst-assisted chemical looping for CO₂ conversion to CO. *Appl. Catal. B Environ.* **2015**, *164*, 184–191. [[CrossRef](#)]
13. Song, T.; Shen, T.; Shen, L.; Xiao, J.; Gu, H.; Zhang, S. Evaluation of hematite oxygen carrier in chemical-looping combustion of coal. *Fuel* **2013**, *104*, 244–252. [[CrossRef](#)]
14. Linderholm, C.; Knutsson, P.; Schmitz, M.; Markström, P.; Lyngfelt, A. Material balances of carbon, sulfur, nitrogen and ilmenite in a 100 kW CLC reactor system. *Int. J. Greenh. Gas Control* **2014**, *27*, 188–202. [[CrossRef](#)]
15. Cocchi, S.; Mari, M.; Cavani, F.; Millet, J.-M.M. Chemical and physical behavior of CoFe₂O₄ in steam-iron process with methanol. *Appl. Catal. B Environ.* **2014**, *152*, 250–261. [[CrossRef](#)]
16. Siriwardane, R.; Tian, H.; Simonyi, T.; Poston, J. Synergetic effects of mixed copper-iron oxides oxygen carriers in chemical looping combustion. *Fuel* **2013**, *108*, 319–333. [[CrossRef](#)]
17. Tseng, Y.-H.; Ma, J.-L.; Chin, C.-P.; Kuo, Y.-L.; Ku, Y. Preparation of composite nickel-iron oxide as highly reactive oxygen carrier for chemical-looping combustion process. *J. Taiwan Inst. Chem. Eng.* **2014**, *45*, 174–179. [[CrossRef](#)]
18. Qiu, Y.; Zhang, S.; Cui, D.; Li, M.; Zeng, J.; Zeng, D.; Xiao, R. Enhanced hydrogen production performance at intermediate temperatures through the synergistic effects of binary oxygen carriers. *Appl. Energy* **2019**, *252*, 113454. [[CrossRef](#)]
19. Qin, L.; Guo, M.; Liu, Y.; Cheng, Z.; Fan, J.A.; Fan, L.-S. Enhanced methane conversion in chemical looping partial oxidation systems using a copper doping modification. *Appl. Catal. B Environ.* **2018**, *235*, 143–149. [[CrossRef](#)]

20. Zhou, H.; Yi, Q.; Wei, G.; Zhang, Y.; Hou, Y.; Huang, Z.; Zheng, A.; Zhao, Z.; Li, H. Reaction performance and lattice oxygen migration of MnFe_2O_4 oxygen carrier in methane-carbon dioxide reaction system. *Int. J. Hydrogen Energy* **2020**, *45*, 30254–30266. [[CrossRef](#)]
21. Sun, Z.; Wu, X.; Russell, C.K.; Dyar, M.D.; Sklute, E.C.; Toan, S.; Fan, M.; Duan, L.; Xiang, W. Synergistic enhancement of chemical looping-based CO_2 splitting with biomass cascade utilization using cyclic stabilized $\text{Ca}_2\text{Fe}_2\text{O}_5$ aerogel. *J. Mater. Chem. A* **2018**, *7*, 1216–1226. [[CrossRef](#)]
22. Huang, Z.; Deng, Z.; Chen, D.; Wei, G.; He, F.; Zhao, K.; Zheng, A.; Zhao, Z.; Li, H. Exploration of Reaction Mechanisms on Hydrogen Production through Chemical Looping Steam Reforming Using NiFe_2O_4 Oxygen Carrier. *ACS Sustain. Chem. Eng.* **2019**, *7*, 11621–11632. [[CrossRef](#)]
23. Chen, J.; Zhao, K.; Zhao, Z.; He, F.; Huang, Z.; Wei, G. Identifying the roles of MFe_2O_4 (M=Cu, Ba, Ni, and Co) in the chemical looping reforming of char, pyrolysis gas and tar resulting from biomass pyrolysis. *Int. J. Hydrogen Energy* **2019**, *44*, 4674–4687. [[CrossRef](#)]
24. Daza, Y.A.; Kent, R.A.; Yung, M.M.; Kuhn, J.N. Carbon Dioxide Conversion by Reverse Water–Gas Shift Chemical Looping on Perovskite-Type Oxides. *Ind. Eng. Chem. Res.* **2014**, *53*, 5828–5837. [[CrossRef](#)]
25. Haeussler, A.; Abanades, S.; Jouannaux, J.; Julbe, A. Non-Stoichiometric Redox Active Perovskite Materials for Solar Thermochemical Fuel Production: A Review. *Catalysts* **2018**, *8*, 611. [[CrossRef](#)]
26. Carrillo, A.J.; Bork, A.H.; Moser, T.; Sediva, E.; Hood, Z.D.; Rupp, J.L.M. Modifying $\text{La}_{0.6}\text{Sr}_{0.4}\text{MnO}_3$ Perovskites with Cr Incorporation for Fast Isothermal CO_2 -Splitting Kinetics in Solar-Driven Thermochemical Cycles. *Adv. Energy Mater.* **2019**, *9*, 13. [[CrossRef](#)]
27. Huang, Z.; Jiang, H.; He, F.; Chen, D.; Wei, G.; Zhao, K.; Zheng, A.; Feng, Y.; Zhao, Z.; Li, H. Evaluation of multi-cycle performance of chemical looping dry reforming using CO_2 as an oxidant with Fe–Ni bimetallic oxides. *J. Energy Chem.* **2016**, *25*, 62–70. [[CrossRef](#)]
28. Lin, Y.; Wang, H.; Huang, Z.; Liu, M.; Wei, G.; Zhao, Z.; Li, H.; Fang, Y. Chemical looping gasification coupled with steam reforming of biomass using NiFe_2O_4 : Kinetic analysis of DAEM-TI, thermodynamic simulation of OC redox, and a loop test. *Chem. Eng. J.* **2020**, *395*, 125046. [[CrossRef](#)]
29. Liu, W. Controlling lattice oxygen activity of oxygen carrier materials by design: A review and perspective. *React. Chem. Eng.* **2021**, *6*, 1527–1537. [[CrossRef](#)]
30. Chen, D.; He, D.; Lu, J.; Zhong, L.; Liu, F.; Liu, J.; Yu, J.; Wan, G.; He, S.; Luo, Y. Investigation of the role of surface lattice oxygen and bulk lattice oxygen migration of cerium-based oxygen carriers: XPS and designed H_2 -TPR characterization. *Appl. Catal. B Environ.* **2017**, *218*, 249–259. [[CrossRef](#)]
31. Liu, F.; Zhao, J.; Xuan, G.; Zhang, F.; Yang, L. Spatial evolution characteristics of active components of copper-iron based oxygen carrier in chemical looping combustion. *Fuel* **2021**, *306*, 121650. [[CrossRef](#)]
32. Zhao, K.; Zheng, A.; Li, H.; He, F.; Huang, Z.; Wei, G.; Shen, Y.; Zhao, Z. Exploration of the mechanism of chemical looping steam methane reforming using double perovskite-type oxides $\text{La}_{1.6}\text{Sr}_{0.4}\text{FeCoO}_6$. *Appl. Catal. B Environ.* **2017**, *219*, 672–682. [[CrossRef](#)]
33. Wang, M.J.; Zhang, S.X.; Xia, M.; Wang, M.K. A Theoretical Study of the Oxygen Release Mechanisms of a Cu-Based Oxygen Carrier during Chemical Looping with Oxygen Uncoupling. *Catalysts* **2022**, *12*, 332. [[CrossRef](#)]
34. Cheng, Z.; Baser, D.S.; Nadgouda, S.G.; Qin, L.; Fan, J.A.; Fan, L.-S. C_2 Selectivity Enhancement in Chemical Looping Oxidative Coupling of Methane over a Mg–Mn Composite Oxygen Carrier by Li-Doping-Induced Oxygen Vacancies. *ACS Energy Lett.* **2018**, *3*, 1730–1736. [[CrossRef](#)]
35. Huang, Z.; He, F.; Chen, D.; Zhao, K.; Wei, G.; Zheng, A.; Zhao, Z.; Li, H. Investigation on reactivity of iron nickel oxides in chemical looping dry reforming. *Energy* **2016**, *116*, 53–63. [[CrossRef](#)]
36. Cao, J.-L.; Wang, Y.; Yu, X.-L.; Wang, S.-R.; Wu, S.-H.; Yuan, Z.-Y. Mesoporous $\text{CuO-Fe}_2\text{O}_3$ composite catalysts for low-temperature carbon monoxide oxidation. *Appl. Catal. B Environ.* **2008**, *79*, 26–34. [[CrossRef](#)]
37. Cao, W.; Tan, O.; Pan, J.; Zhu, W.; Reddy, C.V.G. XPS characterization of $x\alpha\text{-Fe}_2\text{O}_3\text{-(1-x)ZrO}_2$ for oxygen gas sensing application. *Mater. Chem. Phys.* **2002**, *75*, 67–70. [[CrossRef](#)]
38. Dupin, J.-C.; Gonbeau, D.; Vinatier, P.; Lévassieur, A. Systematic XPS studies of metal oxides, hydroxides and peroxides. *Phys. Chem. Chem. Phys.* **2000**, *2*, 1319–1324. [[CrossRef](#)]
39. Wang, D.; Jin, L.; Li, Y.; Hu, H. Partial oxidation of vacuum residue over Al and Zr-doped $\alpha\text{-Fe}_2\text{O}_3$ catalysts. *Fuel* **2017**, *210*, 803–810. [[CrossRef](#)]
40. Aronniemi, M.; Sainio, J.; Lahtinen, J. XPS study on the correlation between chemical state and oxygen-sensing properties of an iron oxide thin film. *Appl. Surf. Sci.* **2007**, *253*, 9476–9482. [[CrossRef](#)]
41. Wei, Y.; Wang, H.; Li, K. Ce-Fe-O mixed oxide as oxygen carrier for the direct partial oxidation of methane to syngas. *J. Rare Earths* **2010**, *28*, 560–565. [[CrossRef](#)]
42. Biesinger, M.C.; Payne, B.P.; Lau, L.W.M.; Gerson, A.; Smart, R.S.C. X-ray photoelectron spectroscopic chemical state quantification of mixed nickel metal, oxide and hydroxide systems. *Surf. Interface Anal.* **2009**, *41*, 324–332. [[CrossRef](#)]
43. Kuhn, J.N.; Zhao, Z.; Felix, L.G.; Slimane, R.B.; Choi, C.W.; Ozkan, U.S. Olivine catalysts for methane- and tar-steam reforming. *Appl. Catal. B Environ.* **2008**, *81*, 14–26. [[CrossRef](#)]
44. Weckhuysen, B.M.; Wang, D.; Rosynek, M.P.; Lunsford, J.H. Conversion of Methane to Benzene over Transition Metal Ion ZSM-5 Zeolites: II. Catalyst Characterization by X-ray Photoelectron Spectroscopy. *J. Catal.* **1998**, *175*, 347–351. [[CrossRef](#)]

45. Zeng, L.; Cheng, Z.; Fan, J.A.; Fan, L.-S.; Gong, J. Metal oxide redox chemistry for chemical looping processes. *Nat. Rev. Chem.* **2018**, *2*, 349–364. [[CrossRef](#)]
46. Liu, S.; He, F.; Huang, Z.; Zheng, A.; Feng, Y.; Shen, Y.; Li, H.; Wu, H.; Glarborg, P. Screening of NiFe₂O₄ Nanoparticles as Oxygen Carrier in Chemical Looping Hydrogen Production. *Energy Fuels* **2016**, *30*, 4251–4262. [[CrossRef](#)]
47. Yang, H.; Gong, L.; Wang, H.; Dong, C.; Wang, J.; Qi, K.; Liu, H.; Guo, X.; Xia, B.Y. Preparation of nickel-iron hydroxides by microorganism corrosion for efficient oxygen evolution. *Nat. Commun.* **2020**, *11*, 5075. [[CrossRef](#)]
48. Louie, M.W.; Bell, A.T. An Investigation of Thin-Film Ni-Fe Oxide Catalysts for the Electrochemical Evolution of Oxygen. *J. Am. Chem. Soc.* **2013**, *135*, 12329–12337. [[CrossRef](#)]
49. Testa-Anta, M.; Ramos-Docampo, M.A.; Comesaña-Hermo, M.; Rivas-Murias, B.; Salgueiriño, V. Raman spectroscopy to unravel the magnetic properties of iron oxide nanocrystals for bio-related applications. *Nanoscale Adv.* **2019**, *1*, 2086–2103. [[CrossRef](#)]
50. Ma, Z.; Zeng, D.; Zhang, S.; Xiao, R. Effect of Supports on the Redox Performance of NiFe₂O₄ in a Chemical Looping Process. *Energy Technol.* **2019**, *7*, 1900374. [[CrossRef](#)]